Acta Materialia 278 (2024) 120247

Contents lists available at ScienceDirect

Acta Materialia

journal homepage: www.elsevier.com/locate/actamat

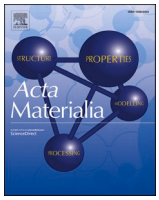

High-performance ultra-lean biodegradable Mg–Ca alloys and guidelines for their processing

Tatiana Akhmetshina [a,*], Leopold Berger [a], Indranil Basu [a], Samuel Montibeller [a], Wolfgang Rubin [a], Andrea M. Rich [a], Robin E. Schäublin [a,b], Jörg F. Löffler [a,*]

[a] Laboratory of Metal Physics and Technology, Department of Materials, ETH Zurich, 8093 Zurich, Switzerland
[b] Scientific Center for Optical and Electron Microscopy (ScopeM), ETH Zurich, 8093 Zurich, Switzerland

ARTICLE INFO

Keywords:
Bioabsorbable Mg
Magnesium alloys
Microstructure
Mechanical properties
Thermo-mechanical processing
Extrusion

ABSTRACT

High-performance *ultra-lean* binary Mg–Ca alloys are engineered by intelligent alloying and thermo-mechanical processing using hot-extrusion. With Ca-alloying contents as low as 0.2-0.6 wt.%, remarkable room-temperature tensile properties are obtained with tensile strength values as high as 380–420 MPa, or ductility values reaching a maximum of 36 %. By means of multiscale structural and chemical analysis using electron microscopy and energy dispersive X-ray spectroscopy, we show that multimodal strengthening mechanisms can be activated by modifying the spatial distribution of Ca as secondary phase. Our results indicate that strong precipitation strengthening is achieved when Mg_2Ca phase particles are dispersed within the grains. On the other hand, preferential distribution of the Mg_2Ca precipitates along grain boundaries imparts substantial grain-boundary strengthening by the Hall-Petch effect. Apart from secondary-phase precipitation, the role of Ca as solute atoms is paramount in promoting homogeneous deformation. The presence of Ca directly alters the intrinsic stacking fault energies and modifies the cross-slip energy barriers such that the slip-transition probability from pyramidal-to-basal and vice-versa becomes comparable. Both effects ensure competitive activation of basal and non-basal slip, thereby reducing the mechanical anisotropy. The mechanical performance in the current work, when compared to earlier reported studies of Mg alloys with similar or higher alloying content, shows a 2 to 10-fold increase in tensile strength without compromising ductility.

1. Introduction

The development of biodegradable implants for bone fracture fixations is of great importance because permanent fixation systems are not always an option. Avoiding a second operation to remove the implants not only ensures cost-effective surgical treatments but also helps avoiding post-operative complications, and related physical and mental trauma among patients [1,2]. Most present-day biodegradable implant materials fall into two main materials groups, namely polymers and metals. However, for load-bearing applications, polymeric implants often fail to provide sufficient mechanical strength to adequately support a fractured bone until it heals. In this respect, metallic implants, such as those based on magnesium, zinc, or iron, perform better mechanically [3]. Among them, magnesium (Mg) offers a unique combination of the required properties: its elastic modulus is close to that of bone (thus limiting the effects of *stress-shielding*), it is abundant in the body and therefore does not display cytotoxicity, and it can be tailored to degrade with an adequate or even adjustable speed [4,5]. In many systems suggested and studied for implant applications [6,7], magnesium is alloyed with other elements, such as with Al, Zn, Mn in "AZ" alloy series, Zr, and rare-earth (RE) elements such as Y and Nd in "WE" alloys [8–10]. The choice of elements is often driven by the quest for strength or formability enhancement. However, a maximum in biological safety, enhanced mechanical properties, and suitable biodegradation performance cannot be mutually exclusive for biomedical applications.

In the past decade, biodegradable lean Mg alloys (with less than 1 wt. % of alloying elements) consisting of only Mg, Zn and Ca have been thoroughly investigated and exhibit promising results [11,12]. However, zinc has recently been shown to accelerate corrosion rate due to its redeposition on the corroding surface, facilitating enhanced cathodic reaction kinetics [13]. In this respect, alloying Mg with only calcium (Ca) is expected to be a more suitable solution, because Ca is less noble than Mg and thus will mitigate corrosion. There is also no potential health hazard because Ca is an important constituent (1 to 2 %) of the

* Corresponding authors.
E-mail addresses: tatiana.akhmetshina@mat.ethz.ch (T. Akhmetshina), joerg.loeffler@mat.ethz.ch (J.F. Löffler).

https://doi.org/10.1016/j.actamat.2024.120247
Received 26 April 2024; Received in revised form 22 July 2024; Accepted 31 July 2024
Available online 31 July 2024

human body, with 99 % of it being in the bones and comprising up to 40 % of them [14]. Some works [15–17] showed that Mg–Ca alloys exhibit even better corrosion resistance than pure Mg. *In vivo* studies on Mg–Ca alloys also showed good biocompatibility and osseointegration [18].

In Mg alloys Ca atoms can either form precipitates made of the hexagonal C14 Mg_2Ca Laves phase [19,20] or remain in solid solution. As precipitates, Ca helps to control grain growth during thermo-mechanical treatment, as it pins grain boundaries [11,21] during dynamic recrystallization. This, in turn, allows maintaining a small grain size, which contributes to the strengthening of the alloy. On the other hand, the presence of Ca as solute atoms is known to provide solid-solution strengthening. The presence of solute Ca also plays a key role in *modifying texture* by weakening the typically observed basal deformation texture in pure Mg [22]. Such an impact has been frequently seen when adding rare-earth elements [23–26], and plays a fundamental role in improving both strength and ductility [27,28].

In addition to effective alloying schemes, tailoring microstructure and mechanical properties also requires intelligent thermo-mechanical processing routes. Among other typical methods used for Mg alloys, hot-extrusion is one of the most convenient and efficient methods for large-scale production. Typical dimensions of the extruded material enable application-oriented implant design, where its shape can be directly tailored to the application. For example, round extrusions are suitable for manufacturing screws, while flat extrusions are more suitable for bone-fixation plates. Bone-fracture fixation systems also demand a wide range of mechanical properties depending on their final application. For example, high strength is useful for inserting screws into bone, whereas high ductility is necessary for forming the plates to match the bone's curvature. Thus, magnesium extrusion research has also strong translational potential in the healthcare industry.

Despite these advantages, systematic studies on extruded Mg–Ca alloys and their corresponding impact on the mechanical properties are still lacking. In this work, we explore potential routes for the mechanical improvement of binary Mg–Ca alloys (X0 series) and attempt to rationalize the synergy of Ca alloying and extrusion parameters. By investigating the process-structure-property relationships across an extensive parameter space, critical recommendations on the design of magnesium implants are presented. The outcomes put forth a new class of *ultra-lean* Mg alloys with exceptional mechanical properties and corrosion resistance.

2. Methods

2.1. Material processing

Alloys were made from Mg with a purity of 99.95 wt.% from Non Ferrum™ and Ca with a purity of 99 wt.% from Sigma-Aldrich. Billets were prepared in an induction furnace at 750 °C under a protective Ar atmosphere. To achieve a homogeneous distribution of Ca, after casting the billets were homogenized at 350 °C for 12 h, then solutionized at 450 °C for 8 hours, and quenched with water or pressurized air.

Hot-extrusion was performed on an instrumented 2.5 Mega Newton extrusion device from Müller Engineering GmbH (Sand/Todtenweis, Germany). Billets were machined into cylinders of 51 mm in diameter to fit the extrusion container dimensions (52 mm). Based upon the prior knowledge of the extrusion response for the ternary alloy ZX00 (0.45 wt. % Zn, 0.45 wt.% Ca) [29], the extrusion parameter space for the binary counterpart Mg-0.45Ca (X0 series) alloy was designed. In order to ensure the presence of the Mg_2Ca intermetallic phase during hot-extrusion (above ~260 °C), the Ca content should be at least 0.15 wt.%. The selected Ca contents for this work were thus chosen as 0.2, 0.3, 0.45 and 0.6 wt.%. Extrusions were performed at temperatures ranging from 280 to 390 °C and at a ram speed between 0.001 and 8 mm s^{-1}. To correlate the processing parameter space with the resulting mechanical properties, a mathematical expression that combines the temperature and strain-rate contribution was utilized. This is expressed as the logarithm of the Zener-Hollomon parameter (ln *Z*) [30], given by:

$$Z = \dot{\varepsilon} \exp\left(\frac{Q}{RT}\right) \tag{1}$$

where $\dot{\varepsilon}$ is the average strain rate, R is the gas constant, T is the deformation temperature, and Q is the activation energy for diffusion (135 kJ/mol for Mg) [30,31]. The average strain rate ($\dot{\varepsilon}$) was defined using the Feltham equation [32], which accounts for the extrusion ratio (area reduction):

$$\dot{\varepsilon} = \frac{6 \ln\left(\frac{D_0^2}{D_{\text{final}}^2}\right) \vartheta_{\text{ram}} D_0^2}{D_0^3 - D_{\text{final}}^3} \tag{2}$$

where ϑ_{ram} is the ram speed, and D_0 and D_{final} are the diameters of the starting and extruded material, respectively.

The extrusion temperatures were selected to retain the Mg_2Ca precipitates in the microstructure, based on the phase diagram calculations using Pandat software [33]. The temperature ranges used for extrusion are shown in Fig. 1a with dotted lines for each composition. The Zener-Hollomon parameter (ln *Z*) is presented in Fig. 1b. The detailed summary of the extrusion parameters can be found in Table S1 (Supplementary Information).

Before extrusion, each billet, together with the extrusion die, was pre-heated for 30 min at the intended extrusion temperature in a convection furnace. Indirect extrusions were performed with a round die of 6 mm in diameter (1:75 extrusion ratio). After extrusions, inductively coupled plasma - optical emission spectrometry (ICP-OES) was performed to determine the Ca content and deviations from the nominal composition.

2.2. Mechanical testing

The evaluation of the mechanical properties included room-temperature uniaxial tensile testing and Vickers hardness measurements. Tensile tests were conducted at room temperature according to ISO 6892–1 (diameter: 4 mm, gauge length: 20 mm, strain rate: 10^{-3} s^{-1}) on a universal testing machine (Schenck Trebel, 100 kN) with two specimens per condition. The error bars in the corresponding plots indicate the range of the measured values (minimum and maximum) and the mean values. For hardness measurements, the extruded rods were cut perpendicularly to the extrusion direction, embedded, and mechanically ground with 4000 grade SiC paper. Vickers hardness (HV1) was measured with a Gnehm Brickers 220 machine applying 1 kg force and averaging 10 indents, and error bars correspond to standard deviations.

2.3. Microscopy

Light microscopy was performed on polished samples, after 10 s of etching with acetic picral etchant, on a Zeiss AxioLAB light microscope. Grain size was calculated using the linear intercept method [34]. To better reveal the topology of the fine-grained microstructures, cleaning cross-section cuts were performed with Ga^+ ions and subsequently imaged in secondary-electron mode inside a dual-beam focused ion-beam (FIB) scanning electron microscope (SEM), Helios 5 UX (Thermo Fisher Scientific). Throughout this work grain size and particle size are reported as *mean value* (*standard deviation*), for example *10.2* (*0.4*).

SEM samples for EBSD analysis were prepared by grinding and polishing with diamond paste down to 0.25 μm. The preparation was finished with broad ion-beam (BIB) milling using a Hitachi IM4000 device. EBSD analysis was conducted in an FEI Quanta 200F FEG-SEM operated at 30 kV and equipped with an EDAX Hikari camera. The measurements were made at a tilt angle of 70° and step size of 0.5 μm. A

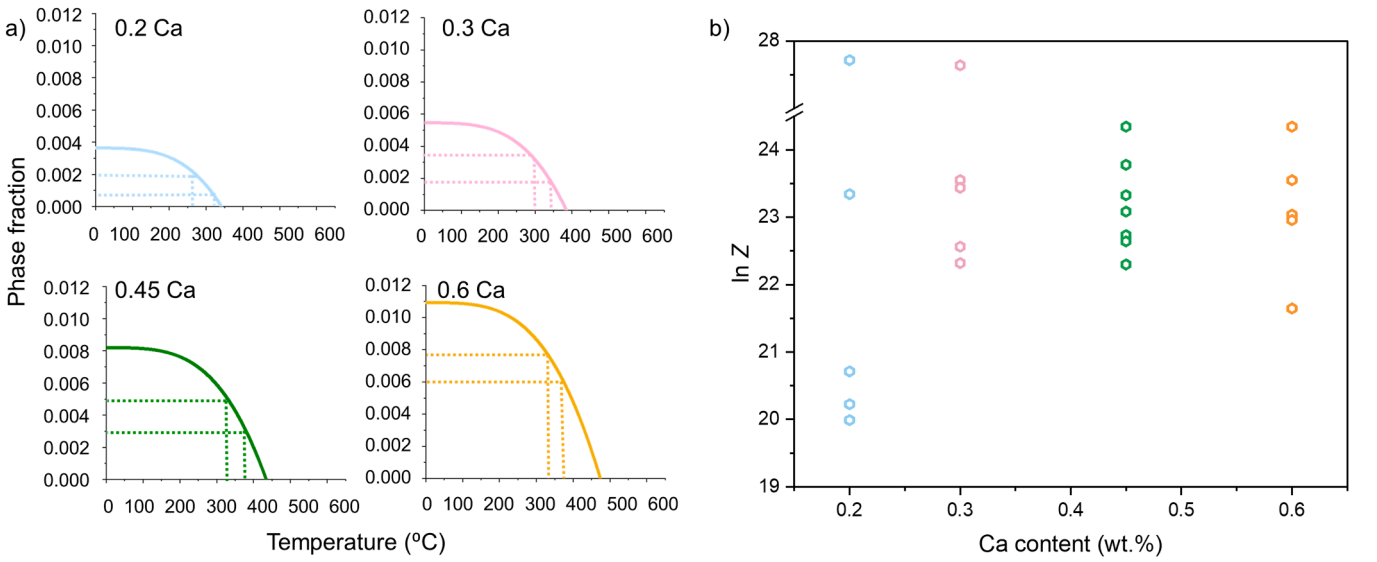

Fig. 1. (a) Calculated Mg_2Ca phase fractions for 0.2 (blue), 0.3 (pink), 0.45 (green) and 0.6 (orange) wt.% Ca. Dotted lines in the phase diagrams show the chosen range of extrusion temperatures and the subsequent phase fraction of the Mg_2Ca precipitates expected at equilibrium. (b) All investigated Zener-Hollomon parameters (ln *Z*), combining average strain rate and temperature, versus Ca content. Color coding as indicated in (a).

hexagonal grid type was implemented.

Samples for TEM examination were mechanically thinned down to 100 μm, then punched into 3 mm diameter disks, and further thinned down to electron transparency with Ar^+ milling using a precision ion-polishing (PIPS II) system from GATAN. Ion milling was performed at a 3.5° incident angle and an acceleration voltage of 4 kV at -70 °C to limit specimen-heating induced changes in the microstructure.

After mechanical testing, sub-micron scale characterization of the deformed microstructure was performed for the most ductile sample (36 % elongation at fracture). A TEM lamella was prepared by FIB milling from the fracture surface of the broken tensile test sample (Fig. S1, Supplementary Information) using standard lift-out and thinning procedures inside a dual-beam TFS Helios 5 UX FIB-SEM. Furthermore, the deformation structure in regions that experienced uniform elongation was assessed. For this, 3 mm TEM discs were extracted from the part of the tensile bar that was approximately 5 mm away from the necking zone and oriented perpendicular to the tensile axis (Fig. S1, Supplementary Information).

TEM and STEM analyses were performed on an FEI Talos™ F200X device equipped with the high throughput Super-X EDS detector of Bruker, yielding a solid angle of 0.9 srad. The device was operated at 200 kV for dislocation analysis. For chemical mapping, which was done over 1024 × 1024 pixels and with a typical acquisition time of 15 min per map, an accelerating voltage of 80 kV was utilized to minimize beam damage and maximize X-ray yield.

The Burgers vector **b** of the dislocations identified from bright-field/dark-field TEM imaging was determined on the basis of the **g**·**b** criterion, where **g** is the operating diffraction vector. Dislocation invisibility is defined by **g**·**b** = 0, while non-zero values indicate visibility. To visualize ⟨*c* ⟩ dislocations in weak-beam bright- and dark-field imaging, the specimens were oriented such that the [10-10] zone axis aligns with the TEM optical axis. On subsequent tilting and imaging at $\boldsymbol{g} = (0002)$, the visible dislocations would thus correspond to ⟨*c*⟩ character. However, when they also show visibility at $\boldsymbol{g} = (11\text{-}20)$, they are identified as ⟨*c* + *a*⟩ dislocations. The density of dislocations (m^{-2}) in non-recrystallized regions was determined with the line-intercept method [44].

High-resolution orientation imaging microscopy (OIM) was performed in TEM using precession electron diffraction (PED). Such an analysis was performed on an FEI Tecnai Osiris TEM operated at 200 kV using the ASTAR™ system by NanoMEGAS [35].

Precipitates were characterized by chemical mapping with STEM EDX. The chemical maps allowed obtaining the precipitates' size (*d*) and number density per unit surface area, N_s. Particle size measurements and counting were performed using CLOCK [36] and ImageJ [37] software programs (Supplementary Information). The thickness, *t*, of the analyzed area was obtained either by stereoscopy [38] or by electron energy loss spectroscopy (EELS) [39] performed on a JEOL F200 operated at 200 kV and equipped with an EELS Continuum spectrometer of GATAN. The number density, *N*, per unit volume was then derived from N_s and *t*. The volume fraction, *f*, of the precipitates' phase was then calculated by summing over the entire size distribution, i.e. the product of the number density, *N*, and the individual precipitate volume, assuming spherical geometry.

3. Results

3.1. Macroscale observations on the extruded Mg–Ca alloys

The extrusion parameters (Fig. 1 and Table S1, Supplementary Information) implemented in this study present optimal results [40] based on macroscale examinations of the surface quality of the extruded rods. Hot-extrusion outside the optimal processing window results in a rough surface finish, indicated by a rippled surface morphology [41] that often acts as a precursor to hot-working induced defects such as premature cracking or hot-tearing. On the contrary, the Mg–Ca extruded rods presented here exhibit a smooth surface finish. While the former roughness stems from poor extrudability induced by mechanical anisotropy in Mg, the absence of it in Mg–Ca alloys hints towards isotropic deformation characteristics that enhance extrudability.

3.2. Mechanical properties of the extruded Mg–Ca alloys

Fig. 2 gives an overview of the mechanical properties of the extruded Mg–Ca alloys under uniaxial tension, measured across all Ca contents selected in this study. A typical plot of ultimate tensile strength (UTS) versus ductility, here defined by elongation at fracture, is shown in Fig. 2a. Conventional materials generally exhibit a trade-off between strength and ductility values, a phenomenon that results in the well-known *banana-shaped* curve [42]. Interestingly, the data values occupying the right end of the plot in Fig. 2a, which correspond to a composition of Mg-0.45Ca, deviate from such a banana-like response. The overall UTS values range from a minimum value of 176 MPa

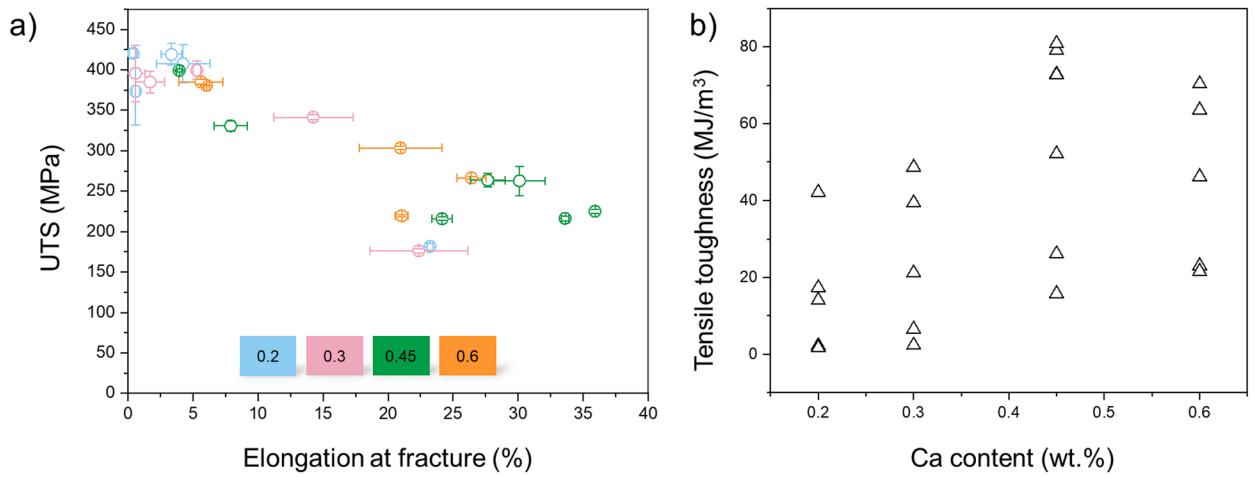

Fig. 2. Mechanical properties of the extruded Mg–Ca alloys: (a) Ultimate tensile stress (UTS) versus ductility (elongation at fracture) ($n = 2$). Color coding corresponds to the Ca content (in wt.%) as indicated in the insets. The data shown are an average with min and max values. (b) Tensile toughness (approximated as UTS times elongation at fracture) as a function of alloy composition.

(corresponding to one extrusion condition for Mg-0.3Ca) to 420 MPa (associated with one of the extruded Mg-0.2Ca alloys). In terms of elongation to fracture, the values reveal an overall improvement for the as-extruded Mg-0.45Ca (4–36 %) and Mg-0.6Ca (6–27 %) alloy series, in comparison to the Mg-0.2Ca (0.4–23 %) and Mg-0.3Ca (0.6–22 %) alloys.

Mechanistically, the extent of strength-ductility trade-off is typically determined by the competitive mechanisms of the material exhibiting strain hardening and the onset of geometric-softening induced plastic instability. Prolonged strain hardening and delayed geometric-softening response directly corresponds to a greater synergy between strength and ductility. A comprehensive parameter to assess the above-mentioned mechanism is the tensile toughness, physically described by the area under the stress-strain curve and mathematically approximated by the product of UTS and elongation to fracture. Fig. 2b shows the related tensile toughness as a function of Ca content. The values indicate that the highest toughness and widest toughness range of 16 – 81 MJ m^{-3} is obtained for the Mg-0.45Ca alloy. In terms of compositional dependence, the toughness values do not display any definitive trend as a function of Ca content, though the values show a slight upward trend for a Ca content up to 0.45 wt.% and a slight reduction when the Ca content is increased further to 0.6 wt.%.

3.3. Correlations between hardness and tensile yield strength of the extruded Mg–Ca alloys

Fig. 3 presents the hardness of the extruded Mg–Ca alloys as a function of their strength. The relationship between strength and hardness for the extruded Mg–Ca alloys follows an expression HV1 = 445.23 + 0.918 TYS (MPa). This deviates from the Tabor relationship of Vickers hardness ≈ three times the yield strength [43] to predict strength from hardness. The Tabor relation typically assumes isotropic plasticity and thus can deviate for materials that exhibit tension-compression yield asymmetry such as Mg [44]. Nevertheless, the relation derived is helpful for a quick estimation of the tensile properties in the Mg-based alloys based on hardness, and the deviation from the Tabor relation hints towards their extent of plastic anisotropy.

3.4. Stress-strain response and correlation with processing parameters for Mg-0.45Ca

Since the mechanical property trends in Fig. 2 revealed the greatest promise for the Mg-0.45Ca alloy, which surpassed other compositions, the present work further focusses on the structure-property correlations

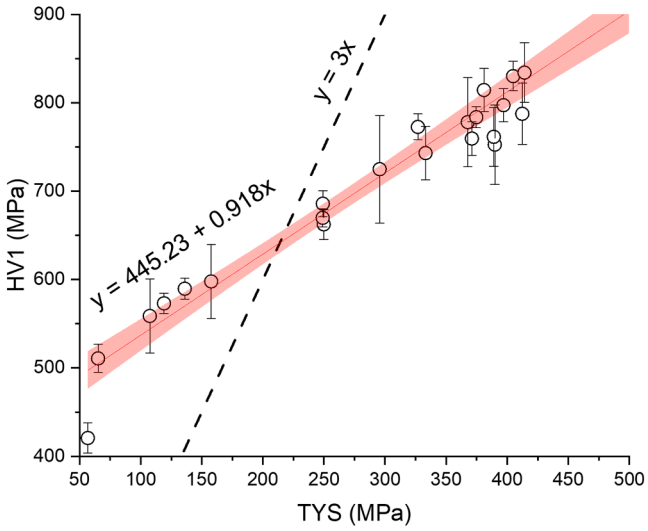

Fig. 3. Relationship between tensile yield strength (TYS) and Vickers hardness (HV1) of the extruded Mg–Ca alloys. The 95 % confidence band (light red) shows the limits of all possible linear fits for the data. The dashed line shows the function $y = 3x$.

in this material.

Fig. 4 shows the uniaxial stress-strain curves for the Mg-0.45Ca alloys extruded across different temperatures and strain rates. The processing parameters are represented by the unified Zener-Hollomon parameter (ln Z). Fig. 4 outlines the potential of tailoring tensile properties by systematically varying the extrusion parameters. The transition from strain softening and yield drop to strain hardening and uniform deformation happens in a narrow window of ln Z ranging from 22.6 to 22.7. Note that the dependence of tensile properties on ln Z is not linear. The potential reasons for such drastic fluctuations with rather minor changes in ln Z will be discussed later on.

3.5. Multiscale microstructural characterization of Mg-0.45Ca alloys

Two extruded Mg-0.45Ca alloys, where one displayed the highest tensile strength and the other showed highest ductility, were probed in terms of microstructure/phase formation and distribution of crystallographic defects. For the sake of brevity, the high-strength and high-ductility Mg-0.45Ca variants are in the following referred to as

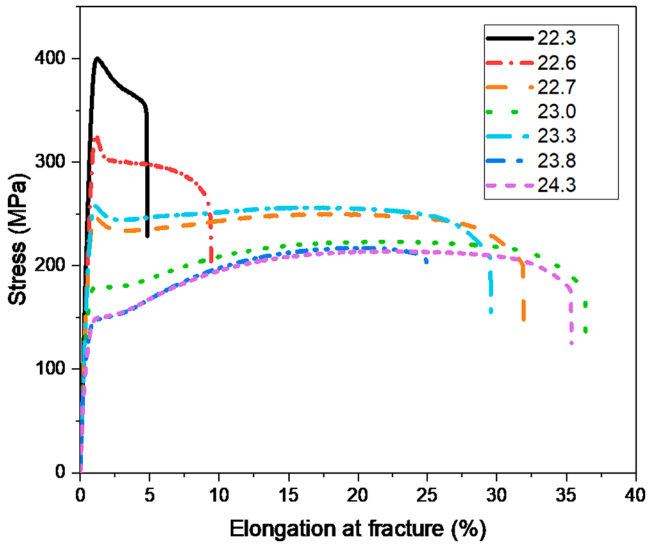

Fig. 4. Engineering stress-strain curves of the extruded Mg-0.45Ca alloys. Extrusion parameters are expressed via the Zener-Hollomon parameter (ln *Z*), yielding a range of ln *Z* values from 22.3 (black solid) to 24.3 (pink short-dashed).

"*strong*-X0" and "*ductile*-X0", respectively.

Light microscopy of the etched microstructures of *strong*-X0 (Fig. 5a-c) shows a partially recrystallized structure composed of elongated unrecrystallized grains (highlighted by yellow arrows) that are aligned with the extrusion direction (ED), and recrystallized colonies of fine equiaxed grains with a diameter of 1.53 (0.22) μm. Light microscopy did not resolve the presence of twinning in the deformed regions or in the intermetallic particles. The measured recrystallized area fraction of as-extruded *strong*-X0 was found to be 48 %. *Ductile*-X0 was extruded at 390 °C (Fig. 5d-f) and exhibits a fully recrystallized microstructure, where equiaxed grains have undergone some recrystallization growth, as evinced by the relatively larger grain size of $d = 4.55$ (1.40) μm.

In order to clearly visualize the fine-grained microstructure in the partially recrystallized regions, Fig. 6a,b presents SEM images of the FIB-cleaning cross-section cuts of the *strong*-X0 alloy. The intermetallic Mg_2Ca particles appear bright. Particles lying within the deformed bands reveal an elongated morphology of up to 500 nm, as highlighted by the blue arrows. The average grain size determined from the SEM images of the *strong*-X0 alloy is 0.86 (0.35) μm, being slightly lower than that measured by optical microscopy. Note that the rippled topography in the SEM images corresponds to FIB-induced curtaining effects that appeared during the cleaning cross-section cuts.

Fig. 6c-e presents bright-field TEM imaging of the deformed bands and neighboring recrystallized grain clusters in the as-extruded *strong*-X0 microstructure. The TEM images show that the deformed bands comprise multiple elongated grains that are separated by low-angle tilt grain boundaries. The average width of individual grains is 200 nm. Imaging at weak-diffraction conditions reveals the precipitate morphology within the bands that seem to preferentially align in the direction normal to the low-angle grain boundaries. Imaging under strong diffraction conditions shows the dislocation substructure within the bands (Fig. 6d). The bands exhibit a dense layered distribution of rectilinear narrow streaks aligned with the basal planes that traverse across the grain width and are identified by an alternating ribbon contrast. Such observations are typical of basal I_1 deformation faults when viewed edge-on. The density of the basal stacking faults was determined as 9.15×10^{13} m^{-2}. Fig. 6d also reveals that the alignment of the elongated block-shaped precipitates is along the identified stacking faults. Additionally, Fig. 6d-e indicates the presence of wavy dislocation lines that are contained within the faults, existing both out-of and within the basal plane, as shown by the green arrows in the magnified image of Fig. 6e. Considering that the operating diffraction vector is $\boldsymbol{g} = (0002)$, the observed dislocations possess <*c*>-character and can be associated with pyramidal $\langle c + a \rangle$ dislocations. The pyramidal dislocation structures also strongly interact with the Mg_2Ca precipitates lying on the basal fault, primarily being blocked at the particle interface, as shown in the magnified image of Fig. 6e.

Fig. 7 presents the Mg_2Ca phase-fraction analysis based on the STEM-EDX elemental maps for *strong*-X0 and *ductile*-X0. Fig. 7a-b shows the corresponding Ca elemental maps. Comparing the EDX maps of the two microstructures, the particle morphology in *strong*-X0 reveals an elongated shape, while a more globular one is found in *ductile*-X0. The measured number density is 4.98×10^{19} m^{-3} and 1.12×10^{19} m^{-3}, and the average particle diameter is 51.6 nm and 85.2 nm, for the *strong*-X0 and *ductile*-X0 specimens, respectively. The resulting molar fractions are 0.00363 for the strong specimen and 0.00290 for the ductile specimen, respectively (see Supplementary Information for more details). Compared to the thermodynamically calculated phase fractions using Pandat, the experimental values indicate deviations, where the measured particle fraction for the *strong*-X0 alloy is lower than the theoretical value (see Fig. 7c). The discrepancies hint towards the role of kinetics that dictate diffusion events along with thermodynamics.

Since the *ductile*-X0 specimen exhibits the highest tensile ductility, fracture surface analysis was performed on the tensile-tested bar. Fig. 8a shows the SEM image of the fracture surface revealing a dimpled morphology, which indicates ductile failure. To investigate the local-scale deformation structure, a lamella was extracted from the fracture surface of the ductile specimen (Fig. 8b). In order to avoid thickness-contrast interference the lamella was thinned down to perforation as shown in Fig. 8c. The micron-scale voids thus appearing in the mid-section and lower-right corner of the lamella are induced from the thinning. Grains at the fracture surface show severe strain-induced distortion and fragmentation (see Fig. 8d-e, g). The large density of accumulated dislocations indicated by the dark contrast areas hints towards a past massive dislocation activity. Grain fragmentation is supplemented by dynamic recovery-induced polygonization events, leading to the formation of dislocation-wall structures, as shown by the green arrows in Fig. 8e. Fragmentation-induced grain refinement resulted in an average reduction of the mean grain size from 4.55 μm (Fig. 8f) to 0.33 μm after tensile deformation (Fig. 8 g).

Fig. 9 shows the dislocation analysis that was performed on the TEM foil obtained from the section of the tensile bar that experienced uniform elongation (Fig. S1, Supplementary Information). Imaging was performed along the $\boldsymbol{g} = (0002)$ diffraction condition to investigate the presence of pyramidal $\langle c + a \rangle$ slip, a critical deformation mode that provides stable strain hardening and enhanced ductility. Fig. 9 indicates the presence of dense dislocation activity inside the grains, all of which possess a $\langle c \rangle$ dislocation character. Since the viewing condition is edge-on with respect to the basal planes, <*c*>-type dislocations that are not aligned with the basal-plane trace lie out of the basal plane while those parallel to the basal trace lie within the basal plane. The out-of-plane dislocation segments are primarily confined to the pyramidal planes. The dislocations reveal a serrated morphology with considerable curving of the dislocation lines. The TEM results in Fig. 9 clearly show substantial activation of <*c*>-type dislocations even at room-temperature deformation in the Mg-0.45Ca alloy. The intermetallic precipitates in the *ductile*-X0 specimen primarily lie at the grain boundaries and hence do not interact with intra-grain dislocation activity.

4. Discussion

4.1. Mechanical properties and extrusion parameters

Our results display a remarkable alloy design scheme, where ultra-lean Ca additions (ranging from 0.2 to 0.6 wt.% Ca) show a massive

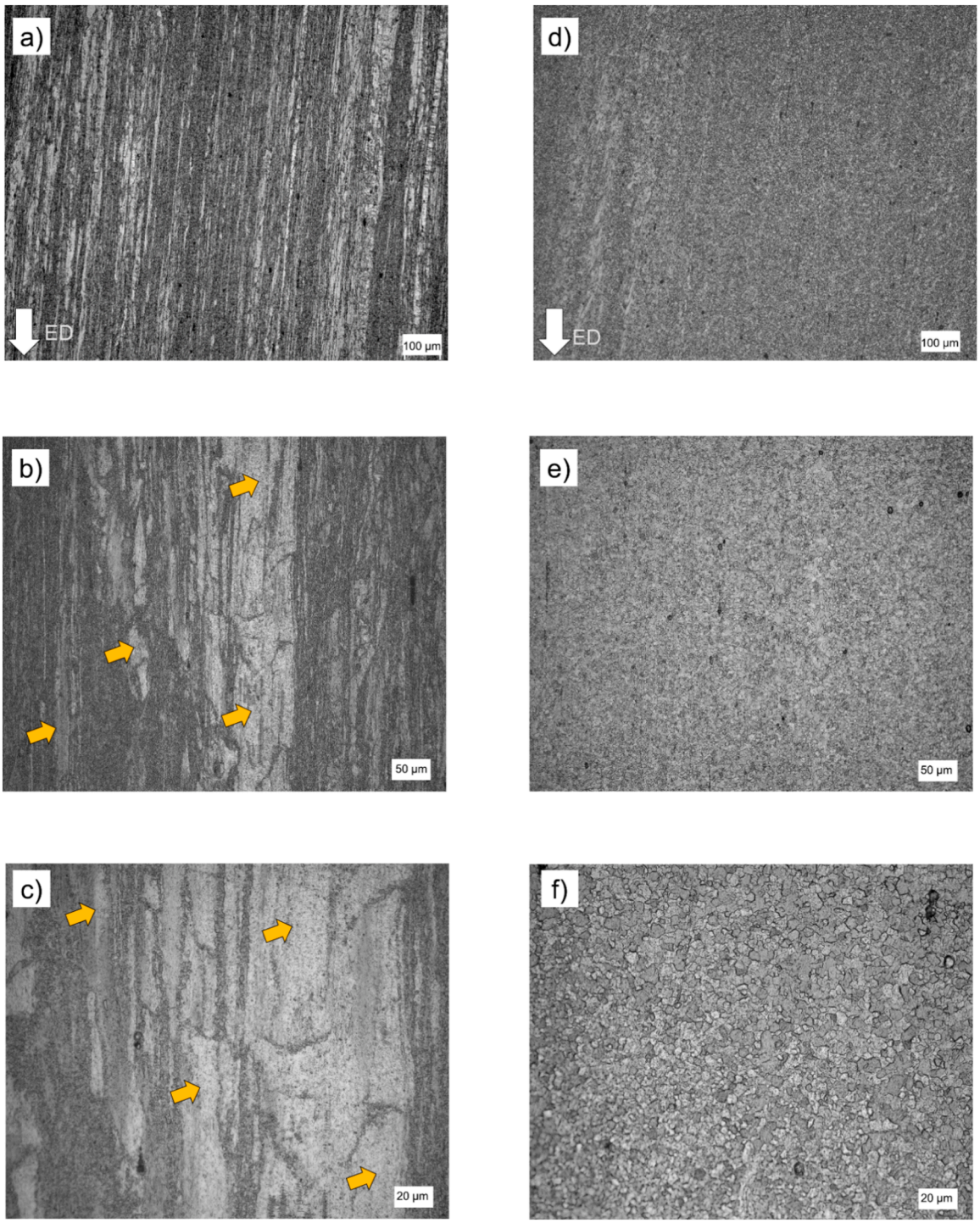

Fig. 5. Microstructures of two Mg-0.45Ca specimens, *strong*-X0 (a-c) and *ductile*-X0 (d-f), parallel to the extrusion direction (ED), as observed with light microscopy. The yellow arrows in (b) and (c) indicate elongated unrecrystallized grains.

impact on strength enhancement, as indicated by the maximum room-temperature UTS values for all compositions that range between 380 MPa and 420 MPa. In comparison, the UTS of extruded pure magnesium typically falls within 210 MPa, as seen for room-temperature deformation [38], and low-temperature [37] and several-pass extrusion [39].

On the other hand, such strength enhancement in binary Mg–Ca alloys does not compromise the material's ductility. Tensile toughness values that combine strength and ductility into a single parameter determine the extent of the material's ability to absorb strain energy until the onset of fracture. The maximum achievable toughness for all Ca additions in the current study range from 40 – 80 MJ m^{-3}. These values are twice that reported for pure Mg subjected to several passes of severe plastic deformation [45]. Apart from the Ca-alloying effect, extrusion processing parameters play a critical role in dictating the final microstructure, which breaks the strength-ductility barrier. Fig. 10 shows contour plots of (a) strength and (b) ductility as a function of the Zener-Hollomon (ln *Z*) parameter and Ca content.

It can be seen that extrusions with ln *Z* below 22.5 result in a high-strength material with more than 400 MPa of UTS, whereas those above 24.5 lead to UTS values below 200 MPa (Fig. 10a). Intermediate

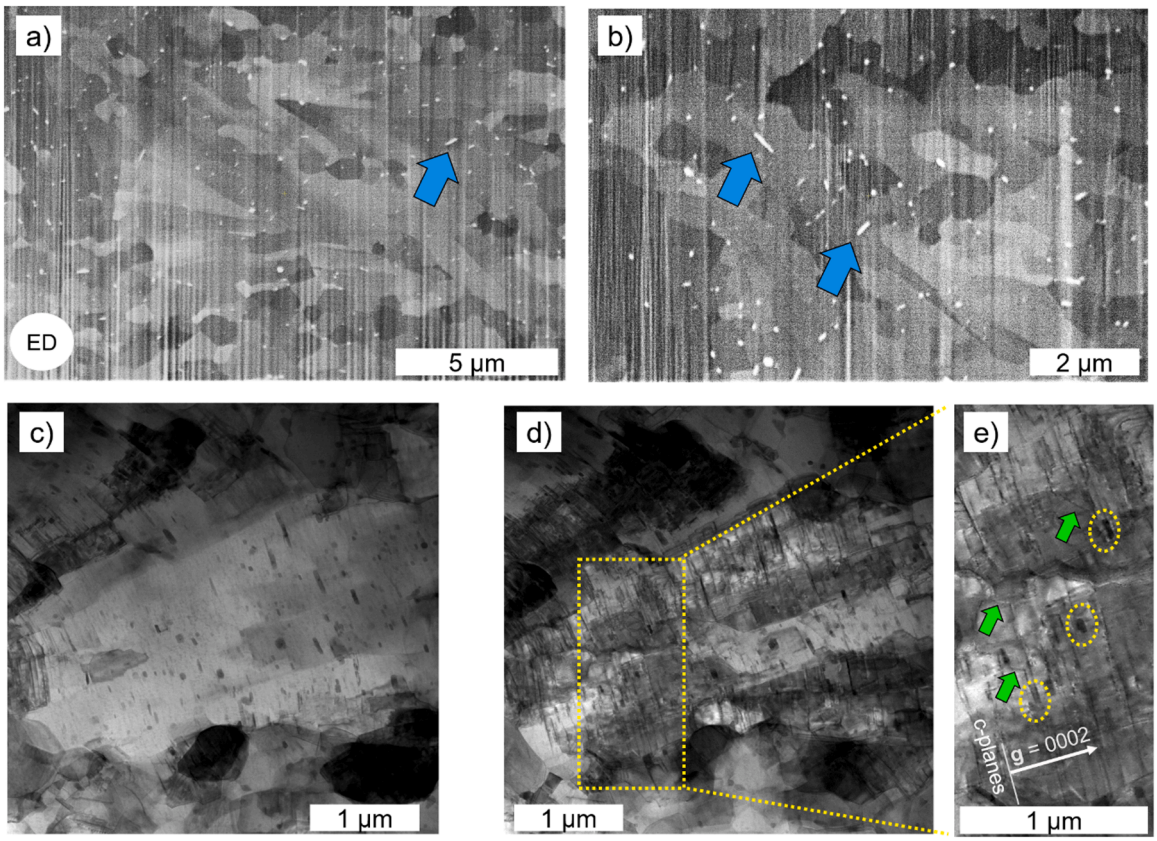

Fig. 6. Electron microscopy images of the Mg-0.45Ca alloy with the highest strength. (a,b) Microstructure after Ga^+ FIB cleaning in secondary-electron (SE) contrast; the blue arrows reveal particles of elongated morphology lying within the deformed bands. "ED" stands for extrusion direction. (c-e) Bright-field TEM images of the same material: (c) weak-diffraction condition revealing precipitates and (d) strong-diffraction condition revealing a large density of dislocations. (e) Magnified view of the inset highlighted in yellow in (d); the green arrows mark inclined pyramidal dislocations and the yellow circles indicate precipitates. The diffraction vector **g** is indicated in (e).

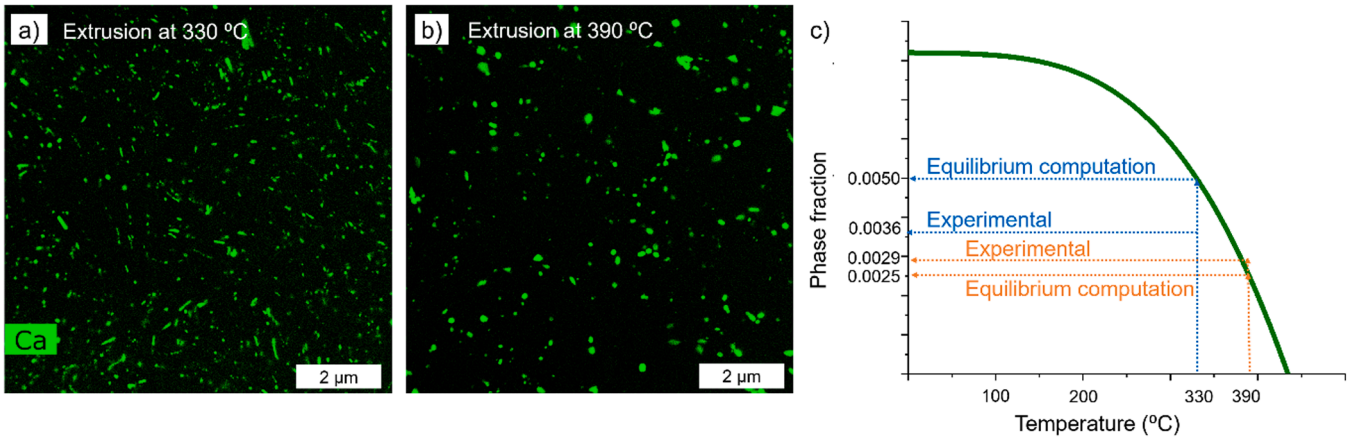

Fig. 7. STEM EDX analysis of (a) *strong*-X0 and (b) *ductile*-X0 alloys. (c) Experimental and Pandat-calculated phase fractions of the secondary phase, Mg_2Ca, shown with dotted lines for the corresponding extrusion temperatures.

ln Z values of 22.5 to 24 yield less predictable properties and a wide range of strength, from 215 to 399 MPa, with an average of 312 MPa. The opposite trend is observed for the elongation at fracture (Fig. 10b), where high ln Z values enhance ductility.

4.2. Deformation mechanisms in Mg-0.45Ca alloys

For the most promising alloying candidate, Mg-0.45Ca (Fig. 4), the stress-strain curves corresponding to low ln Z values of slightly above 22 exhibit high strength (*strong*-X0), which is marked by a short but steep strain-hardening regime that immediately transitions into softening and subsequent failure. In the case of the medium-strength and moderate-ductility Mg-0.45Ca extruded alloys (mid-range value of ln Z ~23), yielding progresses into a short strain-hardening regime that eventually transitions into a stress plateau until failure. On the other hand, high ductility Mg-0.45Ca variants (*ductile*-X0) that were extruded at ln Z values of ~24 indicate a prolonged strain-hardening regime before transitioning into a constant stress state.

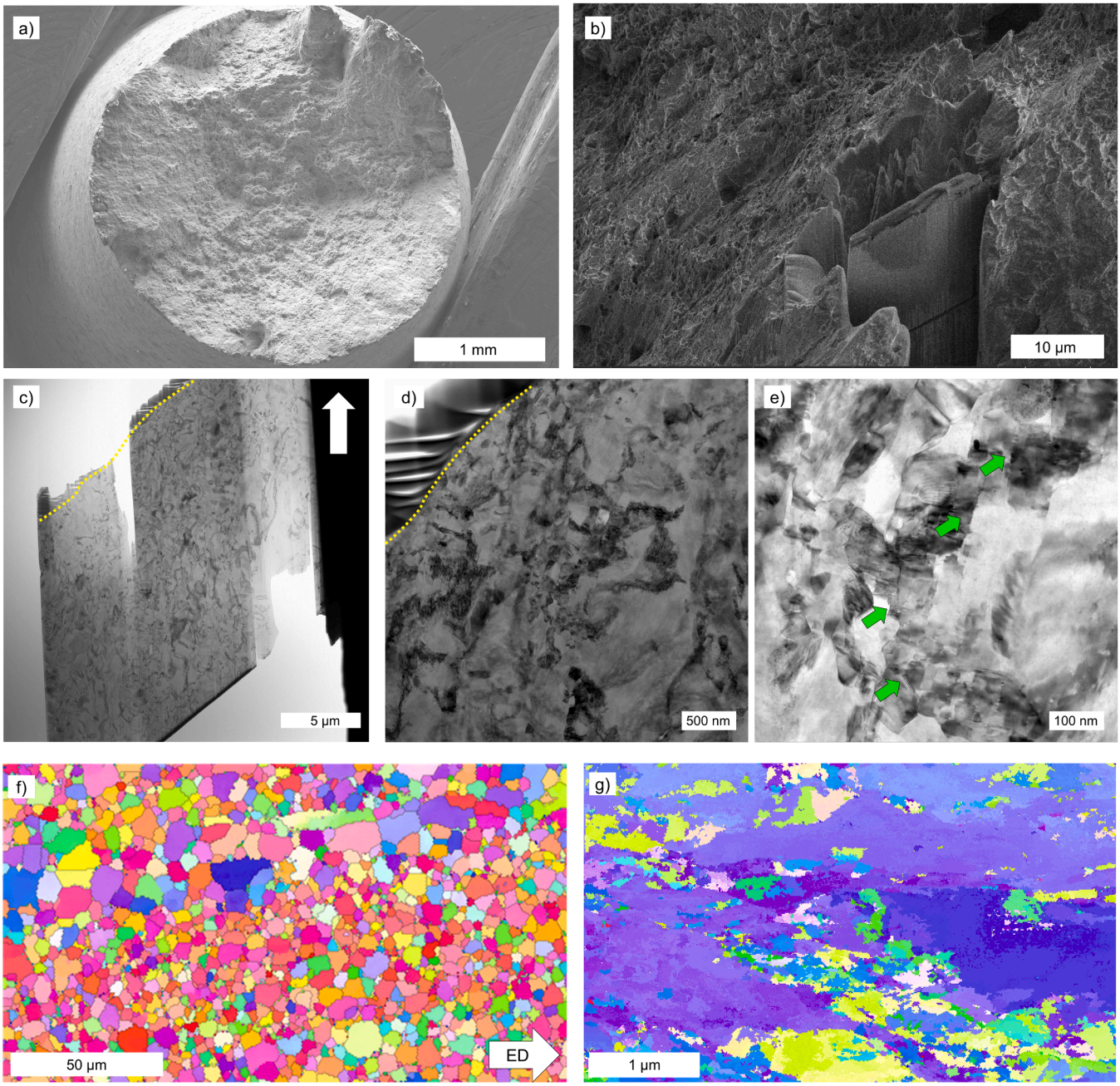

Fig. 8. Analysis of the ductile Mg-0.45Ca specimen after fracture. (a) Fracture surface of the tensile-test specimen and (b) FIB lamella location. (c) The lamella overview with a yellow dashed line indicates the fracture surface; the very top of the surface is protected using carbon deposition. The white arrow indicates the extrusion direction. (d, e) Higher-magnification images, showing (d) elongated lamellar structures with a high density of dislocations and (e) ultra-fine grains below 100 nm; the green arrows in (e) illustrate the occurrence of dislocation-wall structures. (f) EBSD map revealing the grain orientation of the as-extruded state and (g) precession electron diffraction (PED) map revealing the grain orientation of the lamella extracted from the fractured surface.

A universal feature of all the stress-strain curves in Fig. 4 is the appearance of a *concave-up* or sigmoidal hardening curve observed right after plasticity sets in. This is characteristic of twinning-mediated deformation [46,47], where once the critical stress for tension-twin nucleation is reached, twin growth can occur at much lower stresses via low-shear atomic shuffling mechanisms. This corresponds to a strain-softening event in the curve. At the same time, however, twin formation proceeds with a dynamic generation of twin-matrix interfaces that involve large crystallographic reorientations. The formation of such boundaries leads to strong interactions with lattice dislocations, which in turn exert severe latent hardening effects. The twinning-associated rotation into *crystallographically hard* orientations also triggers a strong hardening response. Both phenomena thus produce a transition from softening to a sudden hardening response with the observed sigmoidal behavior.

4.2.1. *Plasticity and strengthening mechanisms of the strong-X0 alloy*

In uniaxial stress-strain tests, isotropic cubic materials generally display distinct plasticity regimes post onset of yielding. As the material yields the stress steadily increases with imposed plastic strain, which is defined as the Stage II strain-hardening regime and mechanistically correlates to strong dislocation-dislocation interactions and dislocation-grain boundary pile-up events. With increasing plastic-strain accommodation the dislocation density rapidly increases, in particular the

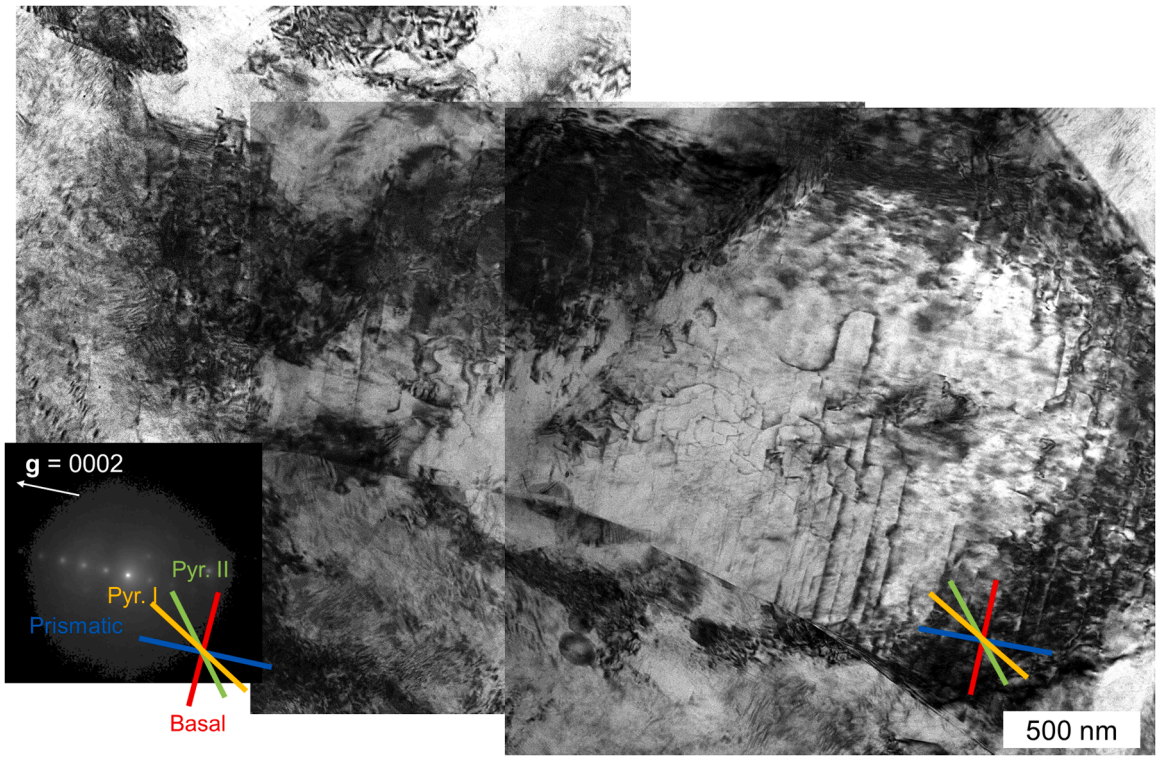

Fig. 9. Dislocation analysis after fracture of the ductile Mg-0.45Ca alloy: bright-field image near a Bragg condition with the operating diffraction vector $\boldsymbol{g} = (0002)$; the diffraction pattern is shown in the inset. Dislocations with a $\langle c \rangle$ component are visible under the two-beam diffraction conditions. The colored lines indicate the trace of (blue) prismatic, (yellow) pyramidal type-I, (green) pyramidal type-II, and (red) basal dislocation glide planes.

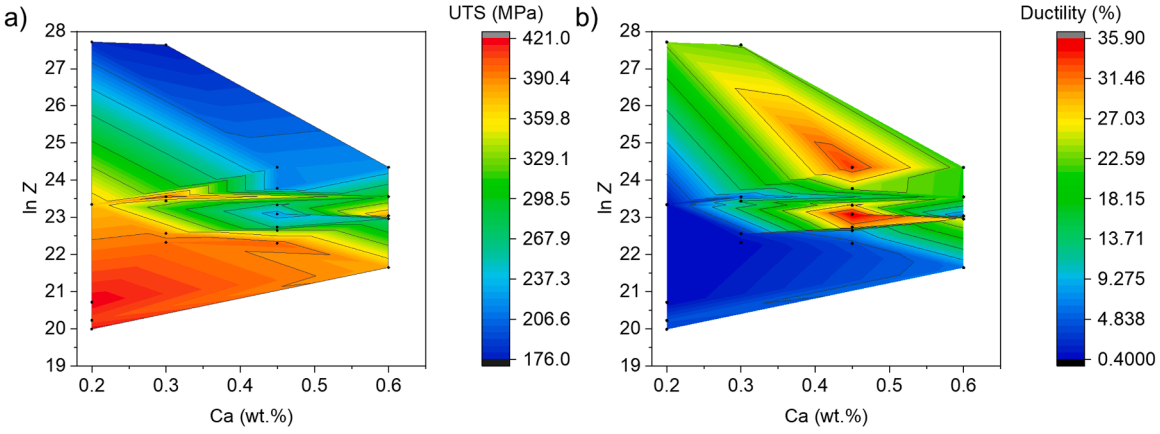

Fig. 10. Contour plots of (a) strength (UTS) and (b) ductility (elongation at fracture) of Mg–Ca alloys as a function of Ca content and extrusion conditions, expressed by the Zener-Hollomon parameter (ln *Z*).

density of the geometrically necessary dislocations, which give way to a Stage III regime highlighted by simultaneous structural rearrangements of dislocations into low-energy configurations. This involves the annihilation of dislocation dipole networks and polygonization of edge dislocations by the activation of cross-slip events. The resultant effect on the stress-strain curve is a drop in the strain-hardening rate and a gradual transition into strain softening, which is induced by the aforementioned dynamic recovery processes [48]. The process of strain softening is atomistically responsible for the generation of vacancies, which macroscopically appears as a local reduction of the cross-sectional area, such that eventually the specimen thickness is not stable enough to sustain plasticity and undergoes failure. It must be noted that the aforementioned dislocation-interaction mechanisms require three-dimensional dislocation structures; they typically occur in a homogeneous von-Mises type deformation.

In the case of *strong*-X0, the as-extruded microstructure is partially recrystallized, where the stored dislocation density in the deformed grains is substantially higher (on the order of $\sim 10^{14}$ m^{-2}, as seen in Fig. 6d,e) compared to the typical values of annealed polycrystals of $\sim 10^{12}$ m^{-2} [49]. Assuming a strengthening coefficient of $\alpha = 0.5$ (typical for metals [50]), the yield-strength increment $\Delta\sigma$ imparted by the pre-existing dislocation density in *strong*-X0 can be evaluated by [51]:

$$\Delta\sigma_{\text{dislocation-hardening}} = \alpha\, G\, \mathbf{b}\, \rho_{\text{GND}}{}^{0.5} \tag{3}$$

where $G\,\mathbf{b}$ is the product of shear modulus and Burgers vector, and ρ_{GND} is the stored dislocation density. Assuming that basal $\langle a \rangle$ dislocations dominantly contribute to the dislocation density, Eq. (3) gives a value of

$\Delta\sigma_{\text{dislocation-hardening}} = 21$ MPa. However, estimating the relative yield-strength increment in *strong*-X0 (~350 MPa) vis-à-vis *ductile*-X0 (~150 MPa) gives a difference of 200 MPa. Here, it is reasonable to define the mechanical response of as-extruded *ductile*-X0 as reference state, because it displays a fully recrystallized structure (analogous to an annealed polycrystalline microstructure), and both alloys do not exhibit significant differences in grain size (0.8–1.5 μm for *strong*-X0 vs. 4.5 μm for *ductile*-X0). The large discrepancy between the mathematically estimated dislocation-density strengthening and the observed strength increment thus suggests an important role of Mg_2Ca particles in the overall strength contribution.

The TEM investigations shown in Fig. 6b-e indicate strong dislocation-particle interactions. The elongated particle morphology along the basal faults within the deformed bands most likely results from a precipitation along dislocation lines. One may expect a strong degree of coherency with the matrix because the angular morphology aligns well with the *c* planes. On the other hand, the $\langle c + a \rangle$ dislocation segments may be strongly blocked by the Mg_2Ca particles, as explained in the following. The observations show a dual-nature dislocation-particle interaction within the Mg–Ca alloys, where both particle-shearing and Orowan-loop driven strengthening mechanisms are active. This is attributed to the inherent asymmetry of the hexagonal crystal structure and to the crystallographic preference of nucleation of the C14-Mg_2Ca phase, which typically precipitates on the close-packed (0002) basal planes of Mg. The corresponding orientation relationship is $(0001)_{C14}||(0001)_{Mg}$ and $[11\text{-}20]_{C14}||[10\text{-}10]_{Mg}$ [52,53]. This results in a directional anisotropy of strain transfer across the incoherent Mg/C14 interphase boundaries, such that slip transfer along the basal plane shows geometric compatibility when moving from the Mg matrix to the Mg_2Ca particles. However, along other non-closed packed planes the interface acts as impenetrable obstacle and thus forces dislocation-looping mechanisms to occur.

In the case of particle shearing by $\langle a \rangle$ dislocations, the strengthening contributions arise from multiple effects such as coherency and modulus hardening, strengthening due to the creation of a new interface, order hardening, and stacking-fault mismatch strengthening (typically relevant for disordered precipitates). In terms of magnitude, the interfacial strengthening contribution is typically negligible [54]. Similarly, coherence and modulus hardening do not fit in this case since the C14 intermetallic phase is structurally incoherent with the matrix. This implies that, unlike for shearing in coherent precipitation, dislocations on the basal plane cannot continue to glide across the interface in the same manner as they shear through the Mg matrix but would need to undergo configurational/structural modifications to sustain plasticity within the Mg_2Ca phase. Such an effect, in some sense, is analogous to slip transfer across geometrically compatible grain boundaries [55]. Hence, the key determining factors in dictating the resistance to strain transfer along basal planes would be the creation of anti-phase boundary sites due to stacking-fault energy fluctuations. I_1-basal stacking faults, when gliding from the matrix into the particle, will undergo a configurational change due to stacking-fault energy variations, where the dissociated Shockley partials recombine into perfect $\langle a \rangle$ dislocations and upon entering the C14 phase give rise to *super-partial* dislocations that enclose an anti-phase boundary domain. Thus, the particle shearing strength would directly be defined by the order-hardening contribution [56]:

$$\Delta\sigma_{\text{particle-shearing}} = \frac{\gamma_{\text{APB}}}{2\mathbf{b}_{\langle a \rangle}}\left(d_{\text{mean}} {N_{\text{V}}}^{1/3} - V_{\text{f}}\right) \tag{4}$$

where γ_{APB} is the anti-phase boundary energy within the C14-Mg_2Ca Laves phase. While the literature presents no experimental values for γ_{APB} in C14-Mg_2Ca, a rough estimate is obtained for a typical C14 crystal structure with $a = 0.497$ nm and $c = 0.81$ nm as 466 mJ m^{-2} (assuming the net-ordering energy that the partials need to overcome for gliding within the C14 particle to be a sum of APB interfacial energy and Peierls frictional stress) [57]. The parameter $\mathbf{b}_{\langle a \rangle}$ is the basal $\langle a \rangle$ Burgers vector within Mg and corresponds to 0.26 nm. Based on the experimental data on volumetric number density N_{V} and particles with volume ${d_{\text{mean}}}^3$, we obtain a total volume fraction $V_{\text{f, total}} = 1/\left({d_{\text{mean}}}^3 N_{\text{V}}\right)$ of 0.00625. Considering that the dislocation-particle interactions are primarily within the unrecrystallized regions that show an intra-grain particle distribution, while the particles within the recrystallized grains preferentially occupy the grain boundaries, we can consider a reduced V_{f} contribution of 0.48 $V_{\text{f, total}}$, which gives $V_{\text{f}} = 0.003$. Substituting the values, we obtain $\Delta\sigma_{\text{particle-shearing}} = 165$ MPa.

In the case of non-basal $\langle c + a \rangle$ dislocations interacting with the Mg_2Ca particles, where the latter act as impenetrable obstacles, we can express the strengthening as [19]

$$\Delta\sigma_{\text{Orowan}} = \frac{2G\mathbf{b}_{\langle c+a \rangle} {V_{\text{f}}}^{0.5}}{d_{\text{mean}}} \tag{5}$$

which gives a value of $\Delta\sigma_{\text{Orowan}} = 21$ MPa. Since the critical yield stress would comply with the larger of the two contributions, i.e. particle shearing or dislocation looping, the strengthening effect from the presence of Mg_2Ca precipitates in the partially recrystallized as-extruded *strong*-X0 alloy is attributed to the order-hardening effect that results in a net particle-induced strengthening of 165 MPa. Thus, combining the contributions of strain hardening from pre-existing dislocations (also 21 MPa, see Eq. (3)) and particle strengthening (165 MPa, see Eq. (4)), the total yield-strength increment is as sum of the two effects equal to 186 MPa. This value stands in reasonable agreement with the aforementioned experimental value of yield-strength difference between *strong*-X0 and *ductile*-X0 of 200 MPa. Thus, the large strengthening effect exhibited by the *strong*-X0 alloy is primarily because of order-hardening effects arising from basal dislocations–C14 phase interactions within the deformed grains. In terms of ductility, the flow curve does not exhibit prolonged strain hardening wherein the sigmoidal feature indicates rapid softening and failure. It is likely that in the presence of Mg_2Ca precipitates, twinning events within the deformed regions give rise to strong twin-particle interactions (such that the particles can block twin propagation) where local stress concentrations can reach high enough values to trigger void nucleation.

4.2.2. *Plasticity and strengthening mechanisms in the ductile-X0 alloy*

The microstructure of the as-extruded *ductile*-X0 alloy exhibits a fully recrystallized grain structure with relatively coarser Mg_2Ca precipitates, which all are distributed along the grain boundaries and triple junctions. The mean grain size of the recrystallized grains is 4.5 μm, which indicates the role of the Mg_2Ca precipitates in effectively pinning grain boundaries and restraining recrystallization growth during hot-extrusion. Although solute Ca can also segregate and pin grain boundaries, this effect is less pronounced than Zener pinning by the Mg_2Ca precipitates due to the easier diffusivity of Ca at the extrusion temperature. To assess the role of grain-boundary pinning on the yielding response, we can express the relative yield-strength increment as a function of grain size using the Hall-Petch relationship:

$$\sigma_y = \sigma_0 + kd^{-0.5} \tag{6}$$

where k is the Hall-Petch coefficient given as 205 MPa μm$^{0.5}$ and σ_0 is 80 MPa, empirically calculated for hot-extruded Mg [58]. Eq. (6) thus gives a yield strength of $\sigma_y \sim 176$ MPa, which is in very good agreement with the experimentally reported yield-stress value of the *ductile*-X0 alloy. In order to exclude potential texture-related stiffness anisotropy that would also impact the yield strength, EBSD maps of the as-extruded microstructures were assessed. These display an almost random texture (see Fig. 8f), which also highlights the role of Ca as a texture modifier, similar to rare-earth elements.

Yielding is followed by a pronounced strain-hardening response reaching a UTS of ~225 MPa. Molar volume fraction calculations showed lower values of Mg_2Ca for *ductile*-X0 compared to *strong*-X0, thus

indicating that part of the alloyed Ca remained in solid solution in the *ductile*-X0 sample. It has been shown in earlier works that Ca solutes exhibit strong segregation propensity to stable and unstable stacking faults in Mg, where they lower the overall stacking fault energy [22,59]. While the lowering of stable stacking fault energy associates with the relative ease of dislocation mobility, the unstable stacking-fault energy contribution dictates the ease of dislocation nucleation. Such energy lowering occurs for both basal stacking faults, i.e. the I_1-growth and I_2-deformation faults. The I_1-growth faults, bound by Frank partials, lead to an out-of-basal plane dissociation and serve as a key source mechanism for $\langle c + a \rangle$ nucleation, which provides five independent deformation modes. The $\langle c + a \rangle$ dislocation nucleation typically occurs via a stair-rod mechanism at the basal-pyramidal plane intersection [59]. Furthermore, the lowering of the stable component of the I_1-growth faults energetically favors sustained glide of pyramidal dislocations and cross-slip of screw components on the pyramidal planes rather than cross-slip into the basal planes. On the other hand, the in-plane I_2-deformation faults that are bound by Shockley partials strengthen basal slip by restricting basal dislocation mobility. This occurs via the formation of extended dislocation structures and restraining the cross-slip of basal dislocations [22,27]. Additionally, the presence of large solutes such as Ca in the Mg lattice can play a pivotal role in modifying the Peierls frictional stress by increasing the local misfit strains, which induces a relative increment in the resolved shear stress to activate basal slip. This also plays a critical role in homogenizing the slip-activation response such that deformation eventually occurs in both the basal and non-basal planes. A similar phenomenon has also been observed for binary Mg–RE alloys [27].

The superposition of the two effects produces a uniform strain-hardening response as observed for the room-temperature tensile test of *ductile*-X0 in Fig. 4. The observation of profuse $\langle c + a \rangle$ slip in Fig. 9 validates such mechanisms. The pyramidal *I* $\langle c + a \rangle$ dislocations glide unhindered between the basal faults and frequently cross-slip into secondary pyramidal *I* planes, which is achieved by an intermediate cross-slip event across the basal plane. Such a cross-slip mechanism is akin to a locking-unlocking mechanism commonly observed for basal $\langle a \rangle$ screw dislocations in pure Mg [60], which transition into another basal plane via an intermediate cross-slip event through the prismatic plane. The interactions of $\langle c + a \rangle$ dislocations with basal dislocations during cross-slip also contribute to work hardening.

Another unique characteristic of plasticity in Mg–Ca alloys is the ease of concurrent cross-slip from pyramidal-to-basal and vice-versa. This is unlikely in pure Mg, where cross-slip can only occur from pyramidal to basal planes due to a much lower energy barrier. Molecular dynamics simulations have shown that for pure Mg the cross-slip energy barrier for pyramidal to basal transition is ~ 0.3–0.5 eV, whereas the cross-slip between pyramidal planes is associated with a higher energy barrier of ~ 0.6–0.9 eV [61–63]. TEM results in the current work (Fig. 9) reveal compelling evidence for cross-slip events between pyramidal and basal planes. This emphasizes the role of Ca in reducing the relative difference in cross-slip energy barriers, such that the propensity of slip transitions from basal-to-pyramidal and pyramidal-to-basal becomes comparable [46,63]. Stable non-basal slip with a glide on multiple pyramidal planes thus becomes possible for Mg–Ca alloys, generating homogeneous deformation and the observed enhanced ductility.

When the tensile stress reaches the UTS in the *ductile*-X0 condition, strain softening does not immediately set in. Rather, the curve exhibits a stress plateau, which continues until an elongation of ~30 %. This indicates a transition from athermal Stage II to Stage III, which involves thermally activated processes, highlighted by the aforementioned cross-slip mechanisms, and also dislocation rearrangements into walls and annihilation of dislocation dipoles. The prolonged Stage III (see Fig. 4) highlights the role of Ca in delaying the onset of uncontrolled geometric softening, where the rate of dynamic recovery would surpass the strain-hardening rate. The presence of Ca solutes within the grains can strongly hinder the glide of dislocations, as they need to overcome the elastic and shear modulus-induced stress fields around the solute environments. At the same time, the presence of Mg_2Ca precipitates at the grain boundaries also retards grain fragmentation and stress-driven grain-boundary migration, both of which would be critical for facilitating continuous dynamic recovery. Transmission EBSD mapping of the fracture surface using precision electron diffraction (PED) inside a TEM revealed stretched and elongated grains that are heavily deformed, but indicated an absence of well-defined sub-grain structures (see Fig. 8 g). The degree of grain refinement pre- and post-deformation was found to change from 4.5 μm to 0.33 μm, indicating an order of magnitude reduction. It is suggested that the onset of recovery-driven inter-granular reorganization is prevented until the Mg_2Ca precipitates are also severely deformed, whereby their pinning resistance is substantially modified. TEM investigations on the fracture surface did not reveal any clear traces of globular Mg_2Ca precipitates and may highlight the effect of repeated shearing events, whereby the particles become extremely fine and, in some cases, may be small enough to re-dissolve into the matrix.

4.3. Comparison of mechanical performance

The current work shows that by intelligent tailoring of the spatial distribution of Ca in rare-earth-free *ultra-lean* Mg–Ca alloys, massive improvements in strength and ductility can be realized over pure Mg and conventional Mg alloys. While Ca as promoter of a secondary phase in the form of Mg_2Ca precipitates can provide an unprecedented strengthening increment, the presence of Ca as solutes plays a key role in intrinsically modifying plasticity response in Mg by triggering competitive activation of basal and non-basal slip modes. Moreover, by modifying the spatial distribution of the Mg_2Ca particles through a strategic choice of thermo-mechanical processing parameters, the strength-ductility synergy can be tailored according to the required application. For instance, in the present study, the intragranular dispersion of Mg_2Ca precipitates generates high-strength Mg alloys, as opposed to the case where they are restricted to the grain-boundary regions and generate a superior strength-ductility synergy. We also compared the mechanical properties of the Mg–Ca alloys tailored in our study with other candidate Mg alloys that have shown great potential and relevance with regard to structural and biomedical applications. Fig. 11 shows their distribution in a ductility versus ultimate tensile strength (UTS) plot, measured per alloying weight (wt.%).

The results were evaluated using the actual Ca content measured

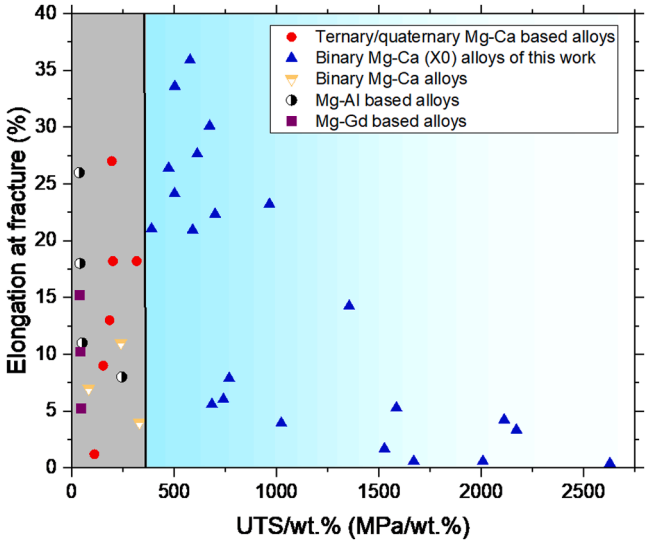

Fig. 11. Increment of strength (UTS) per alloying weight (wt.%) and ductility of Mg–Ca (X0) alloys of this work compared to previously reported wrought alloys of Mg–Ca, ZX, AZ, and Mg–RE alloys (see Table 1 for references).

with ICP-OES and uniaxial engineering stress-strain data. For comparison, we indicate the mechanical properties across various compositions of Mg–Ca, Mg–Zn–Ca (ZX series), Mg–Al–Zn (AZ series), and Mg–RE alloy series that have been reported in the literature (see Table 1). The values indicate that our high-strength Mg–Ca alloy variants show an approximately 10-fold increment with respect to UTS per wt.% of alloying elements (UTS/wt.%) compared to the other alloy compositions. Furthermore, even the most ductile Mg–Ca alloys reported in this work still show a 2-fold increment in the UTS/wt.% compared to the results reported in the literature for other Mg-alloy compositions. Such remarkable mechanical performance, in combination with the excellent biodegradability behavior displayed by the binary Mg–Ca alloys, reveals their huge potential for future biomedical implant applications. [64].

Table 1
Strength increment per alloying content and ductility of various Mg–Ca, ZX, AZ, and Mg–RE alloys.

Alloying elements	Total alloying (wt. %)	UTS (MPa)	UTS/wt.% (MPa/wt. %)	Ductility (%)	Reference
Ca	0.16	420	2628	0.4	This work
Ca	0.39	225	577	36	This work
Ca	1	240	240	11	[18]
Ca	1	330	330	4	[65]
Ca	3	249	83.0	7	[66]
Ca, Sn	4	440	110	1	[67]
Ca, Mn	1.6	322	201	18	[68]
Ca, Al, Zn, Mn	2.3	425	185	13	[69]
Ca, Mn, Zn	2	307	154	9	[70]
Zn, Ca	1.3	255	196	27	[11]
Zn, Ca	0.9	286	317	18	[71]
Al, Ca, Mn	1.13	277	245	8	[41]
Al, Zn	8.5	437	51.4	11	[72]
Al, Zn	10	406	40.6	18	[73]
Al, Zn	10	371	37.1	26	[74]
Gd, Y, Ag, Zr	13	600	46.0	5	[75]
Gd, Y, Zr	7.8	349	44.7	10	[76]
Gd, Y, Zn, Zr	11	442	40.2	15	[77]

5. Conclusions

The present work introduces a new class of hot-extruded *ultra-lean* binary Mg–Ca alloys with alloying additions ranging from 0.2 to 0.6 wt. % (0.15 to 0.43 at.%), which display remarkable room-temperature mechanical properties surpassing those observed for more heavily alloyed Mg alloys. In addition to their superior mechanical properties, their excellent biodegradability properties make them ideal candidates for load-bearing temporary implant applications such as bone-fracture fixation.

By means of detailed microstructural and mechanical characterization, we established key structure-property correlations that are fundamental to the enhanced mechanical response in these alloys. The following main conclusions are derived:

1) *Ultra-lean* binary Mg–Ca alloys by intelligent thermo-mechanical tailoring show maximum achievable room-temperature tensile strength values in the range of 380 – 420 MPa. Furthermore, extended ductility can be achieved in these materials, with selected Mg–Ca alloy variants exhibiting tensile ductility values as high as 36 %.
2) The high strengthening response is attributed to the role of Mg_2Ca precipitates that trigger multimodal strengthening mechanisms based on their spatial distribution. When dispersed within grains (as in the case of the high-strength extruded Mg–Ca variants), the Mg_2Ca precipitates induce strong precipitation hardening, which is dominated by order-hardening effects of the incoming basal dislocations and I_1 faults. Furthermore, the Mg_2Ca precipitates can act as impenetrable obstacles to pyramidal $\langle c+a \rangle$ dislocations, which may force the latter to loop around the precipitates. Such slip-mode dependent dislocation-particle interaction is unique to Mg–Ca alloys, arising from their low crystal symmetry.
3) In the highly ductile as-extruded Mg–Ca alloys the strengthening effect of the Mg_2Ca particles is primarily due to Hall-Petch hardening, as they are preferentially dispersed along the grain boundaries. The dislocation activity within the grains is still modified by the presence of Ca as solute atoms, whereby the intrinsic stacking fault energy is lowered and the cross-slip energy barriers from pyramidal-to-basal and vice-versa become comparable, which facilitates the competitive activation of basal and non-basal slip at ambient temperatures.
4) The materials design scheme in the current work allowed us to successfully engineer extremely lean Mg alloys that exhibit 2–10 times larger strengthening than most counterpart Mg alloys reported in the literature. Furthermore, the reported ductility values also showed a significant increment over those of other Mg alloys.

CRediT authorship contribution statement

Tatiana Akhmetshina: Writing – original draft, Methodology, Investigation, Formal analysis, Data curation, Conceptualization. **Leopold Berger:** Writing – review & editing, Supervision, Methodology, Investigation, Conceptualization. **Indranil Basu:** Writing – review & editing, Methodology, Formal analysis. **Samuel Montibeller:** Writing – review & editing, Investigation, Data curation. **Wolfgang Rubin:** Writing – review & editing, Visualization, Investigation. **Andrea M. Rich:** Writing – review & editing, Investigation. **Robin E. Schäublin:** Writing – review & editing, Supervision, Investigation, Formal analysis, Conceptualization. **Jörg F. Löffler:** Writing – review & editing, Supervision, Methodology, Project administration, Funding acquisition, Conceptualization.

Declaration of competing interest

The authors declare that they have no known competing financial interests or personal relationships that could have appeared to influence the work reported in this paper.

Acknowledgments

The authors thank the Scientific Center for Optical and Electron Microscopy (ScopeM), ETH Zurich for access to its instruments and help with sample preparation. They also thank the Interdisciplinary Centre for Electron Microscopy (CIME), EPFL Lausanne for providing access to its instruments and Dr. Gulnaz Ganeeva for conducting the PED analysis on the TEM Osiris. Financial support by the Swiss National Science Foundation (SNF Sinergia, Grant No. CRSII5- 180367) is gratefully acknowledged.

Supplementary materials

Supplementary material associated with this article can be found, in the online version, at doi:10.1016/j.actamat.2024.120247.

References

[1] J.C.C. Paiva, L. Oliveira, M.F. Vaz, S. Costa-de-Oliveira, Biodegradable bone implants as a new hope to reduce device-associated infections—a systematic review, Bioengineering 9 (2022) 409, https://doi.org/10.3390/bioengineering9080409.
[2] A.F. Mavrogenis, A.D. Kanellopoulos, G.N. Nomikos, P.J. Papagelopoulos, P. N. Soucacos, Early experience with biodegradable implants in pediatric patients, Clin. Orthop. Relat. Res. 467 (2009) 1591–1598, https://doi.org/10.1007/s11999-008-0537-4.

[3] V. Tsakiris, C. Tardei, F.M. Clicinschi, Biodegradable Mg alloys for orthopedic implants – a review, J. Magnes. Alloy. 9 (2021) 1884–1905, https://doi.org/10.1016/j.jma.2021.06.024.

[4] S. Agarwal, J. Curtin, B. Duffy, S. Jaiswal, Biodegradable magnesium alloys for orthopaedic applications: a review on corrosion, biocompatibility and surface modifications, Mater. Sci. Eng. C. 68 (2016) 948–963, https://doi.org/10.1016/J.MSEC.2016.06.020.

[5] F. Kiani, C. Wen, Y. Li, Prospects and strategies for magnesium alloys as biodegradable implants from crystalline to bulk metallic glasses and composites—a review, Acta Biomater. 103 (2020) 1–23, https://doi.org/10.1016/j.actbio.2019.12.023.

[6] M. Pogorielov, E. Husak, A. Solodivnik, S. Zhdanov, Magnesium-based biodegradable alloys: degradation, application, and alloying elements, Interv. Med. Appl. Sci. 9 (2017), https://doi.org/10.1556/1646.9.2017.1.04.

[7] M. He, L. Chen, M. Yin, S. Xu, Z. Liang, Review on magnesium and magnesium-based alloys as biomaterials for bone immobilization, J. Mater. Res. Technol. 23 (2023) 4396–4419, https://doi.org/10.1016/j.jmrt.2023.02.037.

[8] C. Rendenbach, H. Fischer, A. Kopp, K. Schmidt-Bleek, H. Kreiker, S. Stumpp, M. Thiele, G. Duda, H. Hanken, B. Beck-Broichsitter, O. Jung, N. Kröger, R. Smeets, M. Heiland, Improved in vivo osseointegration and degradation behavior of PEO surface-modified WE43 magnesium plates and screws after 6 and 12 months, Mater. Sci. Eng. C. 129 (2021) 112380, https://doi.org/10.1016/j.msec.2021.112380.

[9] S.H. Byun, H.K. Lim, K.H. Cheon, S.M. Lee, H.E. Kim, J.H. Lee, Biodegradable magnesium alloy (WE43) in bone-fixation plate and screw, J. Biomed. Mater. Res. Part B Appl. Biomater. 108 (2020) 2505–2512, https://doi.org/10.1002/jbm.b.34582.

[10] G.W. Mao, H.B. Gong, Y. Wang, X. Li, R. Lv, J. Sun, W.G. Bian, Special Biodegradable Fixation Device for Anterior Cruciate Ligament Reconstruction-Safety and Efficacy in a Beagle Model, ACS Biomater. Sci. Eng. 4 (2018) 3600–3609, https://doi.org/10.1021/acsbiomaterials.8b00426.

[11] J. Hofstetter, M. Becker, E. Martinelli, A.M. Weinberg, B. Mingler, H. Kilian, S. Pogatscher, P.J. Uggowitzer, J.F. Löffler, High-strength low-alloy (HSLA) Mg-Zn-Ca alloys with excellent biodegradation performance, JOM 66 (2014) 566–572, https://doi.org/10.1007/s11837-014-0875-5.

[12] P. Holweg, L. Berger, M. Cihova, N. Donohue, B. Clement, U. Schwarze, N. G. Sommer, G. Hohenberger, J.J.J.P. van den Beucken, F. Seibert, A. Leithner, J. F. Löffler, A.M. Weinberg, A lean magnesium–zinc–calcium alloy ZX00 used for bone fracture stabilization in a large growing-animal model, Acta Biomater 113 (2020) 646–659, https://doi.org/10.1016/j.actbio.2020.06.013.

[13] M. Cihova, E. Martinelli, P. Schmutz, A. Myrissa, R. Schäublin, A.M. Weinberg, P. J. Uggowitzer, J.F. Löffler, The role of zinc in the biocorrosion behavior of resorbable Mg–Zn–Ca alloys, Acta Biomater 100 (2019) 398–414, https://doi.org/10.1016/j.actbio.2019.09.021.

[14] S.M. Garn, Diet and health: implications for reducing chronic disease risk, Am. J. Hum. Biol. 2 (1990) 587–588, https://doi.org/10.1002/ajhb.1310020514.

[15] J.W. Seong, W.J. Kim, Mg-Ca binary alloy sheets with Ca contents of ≤1wt.% with high corrosion resistance and high toughness, Corros. Sci. 98 (2015) 372–381, https://doi.org/10.1016/j.corsci.2015.05.068.

[16] P.R. Cha, H.S. Han, G.F. Yang, Y.C. Kim, K.H. Hong, S.C. Lee, J.Y. Jung, J.P. Ahn, Y. Y. Kim, S.Y. Cho, J.Y. Byun, K.S. Lee, S.J. Yang, H.K. Seok, Biodegradability engineering of biodegradable Mg alloys: tailoring the electrochemical properties and microstructure of constituent phases, Sci. Rep. 3 (2013) 1–6, https://doi.org/10.1038/srep02367.

[17] M. Deng, L. Wang, D. Höche, S.V. Lamaka, C. Wang, D. Snihirova, Y. Jin, Y. Zhang, M.L. Zheludkevich, Approaching "stainless magnesium" by Ca micro-alloying, Mater. Horizons. 8 (2021) 589–596, https://doi.org/10.1039/d0mh01380c.

[18] Z. Li, X. Gu, S. Lou, Y. Zheng, The development of binary Mg-Ca alloys for use as biodegradable materials within bone, Biomaterials 29 (2008) 1329–1344, https://doi.org/10.1016/j.biomaterials.2007.12.021.

[19] R.E. Schäublin, M. Becker, M. Cihova, S.S.A. Gerstl, D. Deiana, C. Hébert, S. Pogatscher, P.J. Uggowitzer, J.F. Löffler, Precipitation in lean Mg–Zn–Ca alloys, Acta Mater 239 (2022) 118223, https://doi.org/10.1016/j.actamat.2022.118223.

[20] S. Amerioun, S.I. Simak, U. Häussermann, Laves-phase structural changes in the system CaAl2-xMgx, Inorg. Chem. 42 (2003) 1467–1474, https://doi.org/10.1021/ic020596m.

[21] K. Huang, R.E. Logé, A review of dynamic recrystallization phenomena in metallic materials, Mater. Des. 111 (2016) 548–574, https://doi.org/10.1016/j.matdes.2016.09.012.

[22] I. Basu, M. Chen, J. Wheeler, R.E. Schäublin, J.F. Löffler, Stacking-fault mediated plasticity and strengthening in lean, rare-earth free magnesium alloys, Acta Mater 211 (2021) 116877, https://doi.org/10.1016/j.actamat.2021.116877.

[23] D. Guan, X. Liu, J. Gao, L. Ma, B.P. Wynne, W.M. Rainforth, Exploring the mechanism of "Rare Earth" texture evolution in a lean Mg–Zn–Ca alloy, Sci. Rep. 9 (2019) 7152, https://doi.org/10.1038/s41598-019-43415-z.

[24] M.G. Jiang, C. Xu, T. Nakata, H. Yan, R.S. Chen, S. Kamado, Development of dilute Mg-Zn-Ca-Mn alloy with high performance via extrusion, J. Alloys Compd. 668 (2016) 13–21, https://doi.org/10.1016/j.jallcom.2016.01.195.

[25] H. Pan, G. Qin, Y. Huang, Y. Ren, X. Sha, X. Han, Z.Q. Liu, C. Li, X. Wu, H. Chen, C. He, L. Chai, Y. Wang, J. feng Nie, Development of low-alloyed and rare-earth-free magnesium alloys having ultra-high strength, Acta Mater 149 (2018), https://doi.org/10.1016/j.actamat.2018.03.002.

[26] N. Stanford, The effect of calcium on the texture, microstructure and mechanical properties of extruded Mg-Mn-Ca alloys, Mater. Sci. Eng. A. 528 (2010) 314–322, https://doi.org/10.1016/j.msea.2010.08.097.

[27] I. Basu, T. Al-Samman, Triggering rare earth texture modification in magnesium alloys by addition of zinc and zirconium, Acta Mater 67 (2014) 116–133, https://doi.org/10.1016/j.actamat.2013.12.015.

[28] J. Hirsch, T. Al-Samman, Superior light metals by texture engineering: optimized aluminum and magnesium alloys for automotive applications, Acta Mater 61 (2013) 818–843, https://doi.org/10.1016/j.actamat.2012.10.044.

[29] N.G. Grün, P. Holweg, S. Tangl, J. Eichler, L. Berger, J.J.J.P. van den Beucken, J. F. Löffler, T. Klestil, A.M. Weinberg, Comparison of a resorbable magnesium implant in small and large growing-animal models, Acta Biomater 78 (2018) 378–386, https://doi.org/10.1016/j.actbio.2018.07.044.

[30] S.S. Park, B.S. You, D.J. Yoon, Effect of the extrusion conditions on the texture and mechanical properties of indirect-extruded Mg-3Al-1Zn alloy, J. Mater. Process. Technol. 209 (2009) 5940–5943, https://doi.org/10.1016/j.jmatprotec.2009.07.012.

[31] J.B. Mann, S. Chandrasekar, W.D. Compton, K.P. Trumble, C. Saldana, S. Swaminathan, G.E. John, W. Moscoso, T.G. Murthy, Severe plastic deformation and the production of nanostructured alloys by machining. Nanostructured Metals and Alloys: Processing, Microstructure, Mechanical Properties and Applications, Elsevier Ltd., 2011, pp. 178–210, https://doi.org/10.1533/9780857091123.1.178.

[32] P. Feltham, Extrusion of metals, Met. Treat. Drop Forg. 23 (1956) 440–444.

[33] W. Cao, S.L. Chen, F. Zhang, K. Wu, Y. Yang, Y.A. Chang, R. Schmid-Fetzer, W. A. Oates, PANDAT software with PanEngine, PanOptimizer and PanPrecipitation for multi-component phase diagram calculation and materials property simulation, Calphad Comput. Coupling Phase Diagrams Thermochem. 33 (2009) 328–342, https://doi.org/10.1016/j.calphad.2008.08.004.

[34] X. Li, L. Cui, J. Li, Y. Chen, W. Han, S. Shonkwiler, S. McMains, Automation of intercept method for grain size measurement: a topological skeleton approach, Mater. Des. 224 (2022), https://doi.org/10.1016/j.matdes.2022.111358.

[35] NanoMEGAS: Advanced Tools for electron diffraction, https://www.nanomegas.com/ (accessed on 31 July 2024).

[36] D.R. Mason, A.E. Sand, X. Yi, S.L. Dudarev, Direct observation of the spatial distribution of primary cascade damage in tungsten, Acta Mater 144 (2018) 905–917, https://doi.org/10.1016/j.actamat.2017.10.031.

[37] C.A. Schneider, W.S. Rasband, K.W. Eliceiri, NIH Image to ImageJ: 25 years of image analysis, Nat. Methods. 9 (2012) 671–675, https://doi.org/10.1038/nmeth.2089.

[38] T.M. Hare, J.C. Russ, J.E. Lane, Volume determination of TEM specimens containing particles or precipitates, J. Electron Microsc. Tech. 10 (1988) 1–6, https://doi.org/10.1002/jemt.1060100102.

[39] R.F. Egerton, Electron Energy-Loss Spectroscopy in the Electron Microscope, Springer US, 2011, https://doi.org/10.1007/978-1-4419-9583-4.

[40] Z. Zeng, N. Stanford, C.H.J. Davies, J.F. Nie, N. Birbilis, Magnesium extrusion alloys: a review of developments and prospects, Int. Mater. Rev. 64 (2019) 27–62, https://doi.org/10.1080/09506608.2017.1421439.

[41] M. Cihova, R. Schäublin, L.B. Hauser, S.S.A. Gerstl, C. Simson, P.J. Uggowitzer, J. F. Löffler, Rational design of a lean magnesium-based alloy with high age-hardening response, Acta Mater 158 (2018) 214–229, https://doi.org/10.1016/j.actamat.2018.07.054.

[42] R.O. Ritchie, The conflicts between strength and toughness, Nat. Mater. 10 (2011) 817–822, https://doi.org/10.1038/nmat3115.

[43] H.E. Boyer, T.L. Gall, Metals Handbook, American Society for Metals, Metals Park, OH, 1985. Desk edition.

[44] P. Zhang, S.X. Li, Z.F. Zhang, General relationship between strength and hardness, Mater. Sci. Eng. A 529 (2011) 62–73, https://doi.org/10.1016/j.msea.2011.08.061.

[45] A. Heydarinia, M. Mohri, P. Asghari-Rad, H.S. Kim, M. Nili-ahmadabadi, Free volume formation and the high strength of pure Mg after room temperature core-sheath ECAP passes, J. Mater. Res. Technol. 18 (2022) 147–158, https://doi.org/10.1016/j.jmrt.2022.02.061.

[46] I. Basu, T. Al-Samman, Hierarchical twinning induced texture weakening in lean magnesium alloys, Front. Mater. 6 (2019) 187, https://doi.org/10.3389/fmats.2019.00187.

[47] M.D. Nave, M.R. Barnett, Microstructures and textures of pure magnesium deformed in plane-strain compression, Scr. Mater. 51 (2004) 881–885, https://doi.org/10.1016/j.scriptamat.2004.07.002.

[48] U.F. Kocks, H. Mecking, Physics and phenomenology of strain hardening: the FCC case, Prog. Mater. Sci. 48 (2003) 171–273, https://doi.org/10.1016/S0079-6425(02)00003-8.

[49] C.M. Cepeda-Jiménez, J.M. Molina-Aldareguia, M.T. Pérez-Prado, Effect of grain size on slip activity in pure magnesium polycrystals, Acta Mater 84 (2015) 443–456, https://doi.org/10.1016/j.actamat.2014.10.001.

[50] A. Rollett, F. Humphreys, G.S. Rohrer, M. Hatherly, Recrystallization and Related Annealing Phenomena: Second Edition, Elsevier Ltd, 2004, https://doi.org/10.1016/B978-0-08-044164-1.X5000-2.

[51] G. Gottstein, Mechanical properties. Physics Found Materials Science, Springer Berlin Heidelberg, Berlin, Heidelberg, 2023, pp. 206–233, https://doi.org/10.5005/jp/books/11061_3.

[52] Z.T. Li, X.G. Qiao, C. Xu, S. Kamado, M.Y. Zheng, A.A. Luo, Ultrahigh strength Mg-Al-Ca-Mn extrusion alloys with various aluminum contents, J. Alloys Compd. 792 (2019) 130–141, https://doi.org/10.1016/j.jallcom.2019.03.319.

[53] J.C. Oh, T. Ohkubo, T. Mukai, K. Hono, TEM and 3DAP characterization of an age-hardened Mg-Ca-Zn alloy, Scr. Mater. 53 (2005) 675–679, https://doi.org/10.1016/j.scriptamat.2005.05.030.

[54] A.J. Ardell, Precipitation hardening, Metall. Trans. A. 16 (1985) 2131–2165, https://doi.org/10.1007/BF02670416.

[55] Z. Shen, R.H. Wagoner, W.A.T. Clark, Dislocation and grain boundary interactions in metals, Acta Metall. 36 (1988) 3231–3242, https://doi.org/10.1016/0001-6160(88)90058-2.
[56] J.J. Bhattacharyya, F. Wang, N. Stanford, S.R. Agnew, Slip mode dependency of dislocation shearing and looping of precipitates in Mg alloy WE43, Acta Mater. 146 (2018) 55–62, https://doi.org/10.1016/j.actamat.2017.12.043.
[57] K.S. Chan, Relationships of fracture toughness and dislocation mobility in intermetallics, Metall. Mater. Trans. A Phys. Metall. Mater. Sci. (2003) 2315–2328, https://doi.org/10.1007/s11661-003-0295-6.
[58] H. Yu, Y. Xin, M. Wang, Q. Liu, Hall-Petch relationship in Mg alloys: a review, J. Mater. Sci. Technol. 34 (2018) 248–256, https://doi.org/10.1016/j.jmst.2017.07.022.
[59] I. Basu, M. Chen, J. Wheeler, R.E. Schäublin, J.F. Löffler, Segregation-driven exceptional twin-boundary strengthening in lean Mg–Zn–Ca alloys, Acta Mater 229 (2022) 117746, https://doi.org/10.1016/j.actamat.2022.117746.
[60] X.Y. Xu, C.P. Huang, H.Y. Wang, Y.Z. Li, M.X. Huang, Rate-dependent transition of dislocation mechanisms in a magnesium alloy, Acta Mater 263 (2024) 119474, https://doi.org/10.1016/j.actamat.2023.119474.
[61] Z. Wu, W.A. Curtin, The origins of high hardening and low ductility in magnesium, Nature 526 (2015) 62–67, https://doi.org/10.1038/nature15364.
[62] R. Ahmad, Z. Wu, S. Groh, W.A. Curtin, Pyramidal II to basal transformation of ⟨c + a⟩ edge dislocations in Mg-Y alloys, Scr. Mater. 155 (2018) 114–118, https://doi.org/10.1016/j.scriptamat.2018.06.026.
[63] Z. Wu, R. Ahmad, B. Yin, S. Sandlöbes, W.A. Curtin, Mechanistic origin and prediction of enhanced ductility in magnesium alloys, Science 359 (80) (2018) 447–452, https://doi.org/10.1126/science.aap8716.
[64] L. Wei, Z. Gao, Recent research advances on corrosion mechanism and protection, and novel coating materials of magnesium alloys: a review, RSC Adv 13 (2023) 8427–8463, https://doi.org/10.1039/d2ra07829e.
[65] H. Pan, G. Qin, Y. Ren, L. Wang, S. Sun, X. Meng, Achieving high strength in indirectly-extruded binary Mg-Ca alloy containing Guinier-Preston zones, J. Alloys Compd. 630 (2015) 272–276, https://doi.org/10.1016/j.jallcom.2015.01.068.
[66] J.W. Seong, W.J. Kim, Development of biodegradable Mg-Ca alloy sheets with enhanced strength and corrosion properties through the refinement and uniform dispersion of the Mg2Ca phase by high-ratio differential speed rolling, Acta Biomater 11 (2015) 531–542, https://doi.org/10.1016/j.actbio.2014.09.029.
[67] H. Pan, G. Qin, Y. Huang, Y. Ren, X. Sha, X. Han, Z.Q. Liu, C. Li, X. Wu, H. Chen, C. He, L. Chai, Y. Wang, J. feng Nie, Development of low-alloyed and rare-earth-free magnesium alloys having ultra-high strength, Acta Mater 149 (2018) 350–363, https://doi.org/10.1016/j.actamat.2018.03.002.
[68] J. She, S.B. Zhou, P. Peng, A.T. Tang, Y. Wang, H.C. Pan, C.L. Yang, F.S. Pan, Improvement of strength-ductility balance by Mn addition in Mg–Ca extruded alloy, Mater. Sci. Eng. A. 772 (2020) 138796, https://doi.org/10.1016/j.msea.2019.138796.
[69] H. Pan, R. Kang, J. Li, H. Xie, Z. Zeng, Q. Huang, C. Yang, Y. Ren, G. Qin, Mechanistic investigation of a low-alloy Mg–Ca-based extrusion alloy with high strength–ductility synergy, Acta Mater 186 (2020) 278–290, https://doi.org/10.1016/j.actamat.2020.01.017.
[70] M.E. Alam, S. Pal, R. Decker, N.C. Ferreri, M. Knezevic, I.J. Beyerlein, Rare-earth- and aluminum-free, high strength dilute magnesium alloy for biomedical applications, Sci. Rep. 10 (2020) 1–15, https://doi.org/10.1038/s41598-020-72374-z.
[71] P. Holweg, L. Berger, M. Cihova, N. Donohue, B. Clement, U. Schwarze, N. G. Sommer, G. Hohenberger, J.J.J.P. van den Beucken, F. Seibert, A. Leithner, J. F. Löffler, A.M. Weinberg, A lean magnesium–zinc–calcium alloy ZX00 used for bone fracture stabilization in a large growing-animal model, Acta Biomater (2020), https://doi.org/10.1016/j.actbio.2020.06.013.
[72] H. Yu, S.H. Park, B.S. You, Development of extraordinary high-strength Mg-8Al-0.5Zn alloy via a low temperature and slow speed extrusion, Mater. Sci. Eng. A. 610 (2014) 445–449, https://doi.org/10.1016/j.msea.2014.05.058.
[73] J. Sun, Z. Yang, J. Han, H. Liu, D. Song, J. Jiang, A. Ma, High strength and ductility AZ91 magnesium alloy with multi-heterogenous microstructures prepared by high-temperature ECAP and short-time aging, Mater. Sci. Eng. A. 734 (2018) 485–490, https://doi.org/10.1016/J.MSEA.2018.07.075.
[74] H.-Y. Wang, Z.-P. Yu, L. Zhang, C.-G. Liu, M. Zha, C. Wang, Q.-C. Jiang, Achieving high strength and high ductility in magnesium alloy using hard-plate rolling (HPR) process, Sci. Rep. 5 (2015) 17100, https://doi.org/10.1038/srep17100.
[75] W.W. Jian, G.M. Cheng, W.Z. Xu, H. Yuan, M.H. Tsai, Q.D. Wang, C.C. Koch, Y. T. Zhu, S.N. Mathaudhu, Ultrastrong Mg alloy via nano-spaced stacking faults, Mater. Res. Lett. 1 (2013) 61–66, https://doi.org/10.1080/21663831.2013.765927.
[76] S. Lu, D. Wu, M. Yan, R. Chen, Achieving high-strength and toughness in a Mg-Gd-Y alloy using multidirectional impact forging, Materials 15 (2022), https://doi.org/10.3390/ma15041508.
[77] X. Jin, W. Xu, D. Shan, B. Guo, B.C. Jin, Mechanism of high-strength and ductility of Mg-RE alloy fabricated by low-temperature extrusion and aging treatment, Mater. Des. 199 (2021) 109384, https://doi.org/10.1016/j.matdes.2020.109384.